catalysts

MDPI

Article

Acidity-Reactivity Relationships in Catalytic Esterification over Ammonium Sulfate-Derived Sulfated Zirconia

Abdallah I. M. Rabee [1,2] (ID)**, Gamal A. H. Mekhemer [1], Amin Osatiashtiani [2]** (ID)**, Mark A. Isaacs [2]** (ID)**, Adam F. Lee [2]** (ID)**, Karen Wilson [2,*] and Mohamed I. Zaki [1]**

[1] Chemistry Department, Faculty of Science, Minia University, El-Minia 61519, Egypt; aimoftah@mu.edu.eg (A.I.M.R.); gmekhemer@mu.edu.eg (G.A.H.M.); mizaki@mu.edu.eg (M.I.Z.)
[2] European Bioenergy Research Institute, Aston University, Birmingham B4 7ET, UK; a.osatiashtiani@aston.ac.uk (A.O.); m.isaacs@aston.ac.uk (M.A.I.); a.f.lee@aston.ac.uk (A.F.L.)
* Correspondence: k.wilson@aston.ac.uk

Abstract: New insight was gained into the acidity-reactivity relationships of sulfated zirconia (SZ) catalysts prepared via $(NH_4)_2SO_4$ impregnation of $Zr(OH)_4$ for propanoic acid esterification with methanol. A family of systematically related SZs was characterized by bulk and surface analyses including XRD, XPS, TGA-MS, N_2 porosimetry, temperature-programmed propylamine decomposition, and FTIR of adsorbed pyridine, as well as methylbutynol (MBOH) as a reactive probe molecule. Increasing surface sulfation induces a transition from amphoteric character for the parent zirconia and low S loadings <1.7 wt %, evidenced by MBOH conversion to 3-hydroxy-3-methyl-2-butanone, methylbutyne and acetone, with higher S loadings resulting in strong Brønsted-Lewis acid pairs upon completion of the sulfate monolayer, which favored MBOH conversion to prenal. Catalytic activity for propanoic acid esterification directly correlated with acid strength determined from propylamine decomposition, coincident with the formation of Brønsted-Lewis acid pairs identified by MBOH reactive titration. Monodispersed bisulfate species are likely responsible for superacidity at intermediate sulfur loadings.

Keywords: zirconia; sulfated zirconia; solid acid; XPS; IR; esterification

1. Introduction

Zirconium oxide (ZrO_2) is an attractive catalyst support owing to its amphoteric surface properties and high hydrothermal and thermal stability. These properties have found catalytic application in, for example, the isomerization of glucose to fructose [1], and the synthesis of dimethyl carbonate [2]. The chemical functionalization of zirconia surfaces with sulfate ions to generate SO_4/ZrO_2 (SZ) solid acid catalysts has attracted significant industrial and academic interest. Early research focused on exploiting the strong (even super-) acidic properties of SZ for gas phase cracking and isomerization of hydrocarbons; however, catalytic applications have expanded in recent years to include liquid phase green chemical processes such as free fatty acid esterification and triglyceride transesterification [3,4], Friedel-Craft alkylation [5], alkane and terpene isomerization [6,7], sorbitol dehydration [8], and glucose conversion to HMF [1]. The promising performance of SZ for these catalytic transformations is mainly attributed to its strong solid acidity and good thermal stability, which are strongly influenced by the sulfation method, sulfur content, and calcination temperature [9].

Identifying and quantifying the active sites are essential to improving our understanding of structure–function relationships, and hence contribute to the design of improved heterogeneous catalysts. However, despite extensive research, the exact nature of active sites in SZ (and how to tune

these) remains an open question. It has been suggested that superacidity arises from Lewis acid sites associated with coordinatively unsaturated zirconium cations [10], whose acid strength is strongly enhanced by the electron withdrawing power of SO_x groups. In contrast, Babou et al. [11] considered the active sites as sulfuric acid molecules grafted onto zirconia, while Chen and co-workers [12] attributed superacidity to a specific sulfate species independent from the sulfur loading. Arata and Hino [13] attributed the superacidity of SZ to the uptake of water on undercoordinated Lewis acid sites, while Clearfield et al. [14] proposed that superacidity arose from a synergy between bisulfate and adjacent Lewis acid sites. According to the latter model, the Brønsted acidity of bisulfate groups is enhanced by the electron-withdrawing character of neighboring Lewis acid sites, thereby weakening the SO-H bond; however, this model is questionable since the electronegativity of Zr^{4+}, and hence its Lewis acidity, is no higher than that of Fe^{3+} and Ti^{4+}, whose sulfated analogues are much weaker acids than SZ [15].

Bensitel et al. [16] found that only tridentate sulfate species Zr_3SO_4 existed on the surface of dehydrated SZ at low S loadings, converting to a bridging bisulfate species in the presence of moisture. These bridging bisulfate species have been suggested as responsible for superacidity. High sulfate loadings are believed to generate polysulfate species in SZ, whose formation Morterra and co-workers [17] propose lowers the corresponding activity in acid catalysis [1].

Previous investigations of different sulfating agents for synthesizing SZ from wet impregnation of $Zr(OH)_4$ have reported that superacidity and associated catalyst activity for 1-butene isomerization are independent of the choice of sulfur source [9]. In light of this report, and the corrosive nature and problematic handling of sulfuric acid, ammonium sulfate appears to be an attractive sulfating agent with which to prepare SZ catalysts. However, to date there are no studies systematically exploring the structure/acidity-activity relationships in SZ synthesized from $(NH_4)_2SO_4$ for liquid phase catalysis. Accordingly, here we study the evolution of surface sulfate species and solid acidity with sulfur loading for ammonium sulfate-derived materials, employing complementary reactive acid probes (propylamine decomposition and methylbutynol isomerization/dehydration) to quantify acid-base, redox and Brønsted-Lewis character. The resulting physicochemical properties are correlated with activity towards propanoic acid esterification, with methanol to elucidate the nature of the active acid sites and their optimization.

2. Results and Discussion

2.1. Catalyst Characterization

Successful genesis of SZ catalysts with a systematic variation in S content from $(NH_4)_2SO_4$ impregnation was first assessed by elemental (CHNS) and XPS analyses to quantify bulk and surface S content, respectively. Table 1 shows that the bulk and surface S loadings increased monotonically with $(NH_4)_2SO_4$ concentration during impregnation. The surface S loading was higher than the bulk, indicating preferential surface functionalization.

Table 1. Physicochemical properties of parent and sulfated zirconia.

| Sample	Surface Area $(m^2 \cdot g^{-1})$	Bulk S Loading [a] (wt %)	Surface Composition [b] (atom %)		S:Zr [c] Atomic Ratio
			S	Zr	
0SZ	40	0.0	0.0	30.9	0.00
1SZ	100	0.9	2.5	29.7	0.08 (0.03)
2SZ	121	1.7	3.5	27.9	0.13 (0.05)
3SZ	90	3.1	4.0	26.1	0.16 (0.10)
4SZ	49	4.6	4.7	26.6	0.18 (0.14)
5SZ	34	5.3	5.6	25.8	0.22 (0.16)

[a] Determined via CHNS analysis; [b] Determined via XPS analysis; [c] Values in parentheses from CHNS.

Figure 1 shows the corresponding powder XRD patterns of SZ catalysts as a function of bulk S loading, which reveal a strong influence on crystallinity. The parent zirconia comprised predominantly (monoclinic) *m*-ZrO_2, with only a very small contribution from (tetragonal) *t*-ZrO_2. In contrast, sulfated samples were dominated by *t*-ZrO_2 with only a weak contribution from the monoclinic phase, as previously reported [18,19]. A gradual weakening of the *t*-ZrO_2 reflections was observed for S loadings ≥3.10 wt %, which has previously been attributed to the formation of amorphous, bulk $Zr(SO_4)_2$ [20]. It is noteworthy that sulfation by sulfuric acid was observed to cause a complete loss of crystallinity for S loadings of 3 wt % [1], highlighting the benefits of $(NH_4)_2SO_4$ as a more mild sulfating agent that preserves structural order.
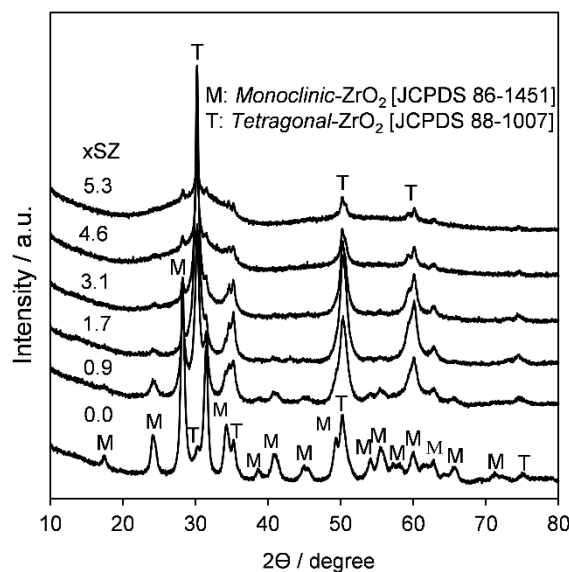
Figure 1. XRD patterns of parent and sulfated zirconia as a function of bulk S loading.

Thermal stability of surface sulfate species were explored by TGA-MS (Figure 2), with the corresponding mass losses summarized in Table 2 along with the nature of species evolved at each temperature. The parent zirconia exhibited a total mass loss of 2.11% upon heating to 1000 °C, principally arising from low-temperature physisorbed water and hydroxyl desorption <350 °C, with an additional mass loss of 0.46 wt % occurs between 350 °C and 600 °C. Sulfated samples also exhibited low temperature water desorption (albeit much greater than for the parent presumably due to hydrogen bonding with surface acid sites) shown in Figure S1, which increased with S loading (Table 2), Figure 2a reveals an additional, large high-temperature mass loss at 600–1000 °C, which was proportional to sulfate loading. Corresponding DTGA and MS data (Figure 2b–c) show that for S loadings ≤0.9 wt % this decomposition occurs in a broad state centered ~870 °C associated with SO_2 desorption. This desorption broadens and shifts to a slightly lower temperature (820 °C) for loadings ≥1.7 wt %, coincident with the emergence of an additional low-temperature desorption associated with the evolution of SO_3 (80 amu, Figure 2d), suggesting the formation of a distinct, new surface sulfoxy species at high loadings, possibly reflecting a change in sulfate coordination on the crowded surface from bidentate to monodentate [7].
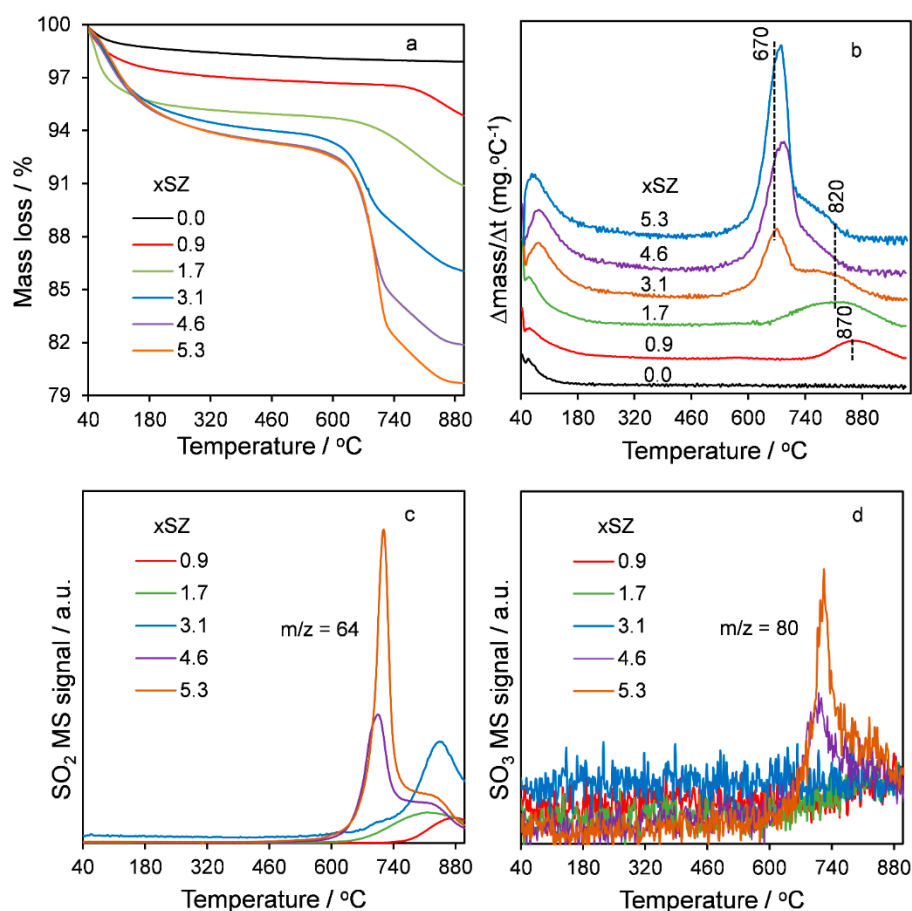
Figure 2. (**a**) TGA and (**b**) DTGA profiles, and temperature-programmed desorption spectra of evolved (**c**) SO_2 and (**d**) SO_3 from parent and sulfated zirconia as a function of bulk S loading.

Table 2. Thermogravimetric-mass spectrometry of parent and sulfated zirconia.

S Content (wt %)	Mass Loss ($\pm$0.1) (%)		Evolved Species [b]
	40–350 °C	600–1000 °C [a]	
0.0	1.42	0.21	H_2O (80–350 °C)
0.9	2.53	1.94 (0.97)	
1.7	3.42	3.73 (1.86)	H_2O, SO_2 (840–870 °C)
3.1	5.00	7.45 (3.73)	
4.6	5.80	9.99 (4.99)	H_2O, SO_2, SO_3 (670 °C)
5.3	5.30	11.89 (5.95)	

[a] Values in parentheses correspond to S loading derived from %mass loss assuming sulfate decomposition to SO_2. [b] Values in parentheses correspond to the temperature of detection by MS.

Considering the possible conformations for surface bound sulfates on zirconia [9,21] (Scheme 1), tridentate (species I) and bidentate bridging (species II) are expected to be the most stable, decomposing >800 °C. Such conformations, particularly bisulfate species II, are consistent with the observation of strong SO_2 desorption for S loadings ≤1.7 wt %.
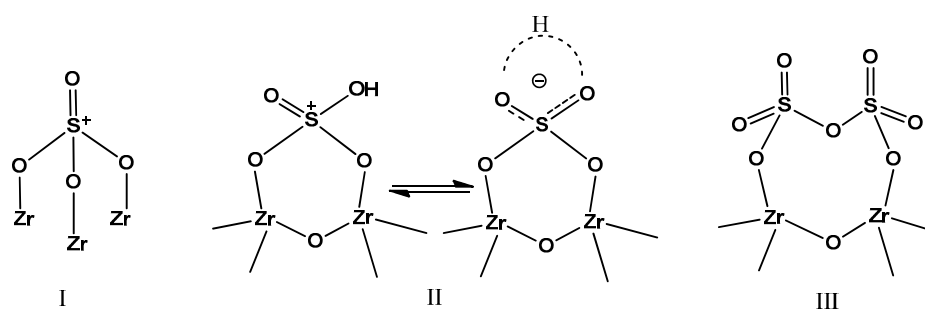
Scheme 1. Possible sulfate configurations for sulfated zirconia.

Bisulfates are known to react around 500 °C via $2HSO_4^- \rightarrow S_2O_7^{2-} + H_2O$ to form polysulfates such as the pyrosulfate anion $S_2O_7^{2-}$ [22], which subsequently decompose at higher temperatures to yield SO_4^{2-} and SO_3 via $S_2O_7^{2-} \rightarrow SO_4^{2-} + SO_3$. Accordingly, we associate the observation of SO_3 desorption around 670 °C for S loadings $\geq$4.6 wt % with pyrosulfate-like species III.
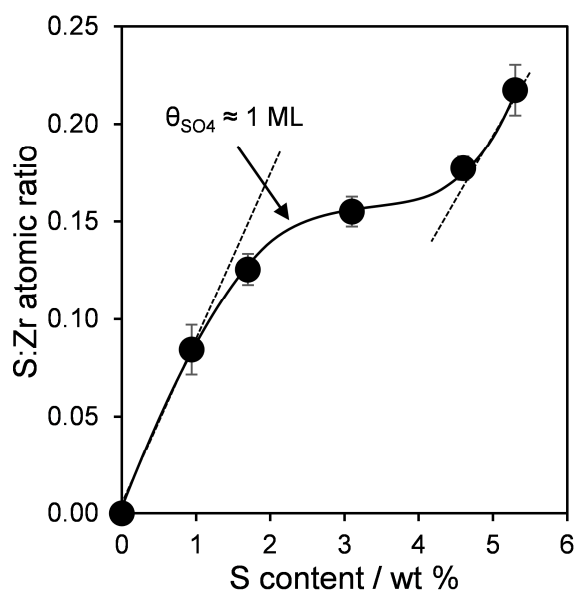
The nature of surface sulfoxy was further explored by XPS. Figure 3 shows the Zr 3d region of parent and sulfated zirconia as a function of S loading, which reveals a progressive increase in Zr $3d_{5/2}$ binding energy from 181.9 $\rightarrow$ 182.5 eV for sulfated samples [23]. This chemical shift is attributed to the electron-withdrawing effect of sulfate groups, and hence an increase in initial state charge (and Lewis acidity) in Zr^{4+} species. The S $2p_{3/2}$ binding energy was around 169–170 eV for all samples (Figure S2a), consistent with SO_4 formation [1,7], and, as previously reported, exhibited a small increase with S loading (from 169.0 $\rightarrow$ 169.4 eV) previously attributed to the genesis of co-existing bidentate and monodentate SO_4 species due to lateral interactions on the crowded surface, reducing the extent of charge-withdrawal from the zirconia substrate. O 1s spectra (Figure S2b) show that sulfation induces a similar small shift to higher binding energy in the surface oxygen species from 529.7 $\rightarrow$ 530.3 eV (Figure S2), accompanied by the growth of a second, high binding chemical state at 531.65 eV attributed to surface hydroxyls. The peak shift is attributed to a transition in the local environment of oxygen from zirconium to the more electronegative sulfur.
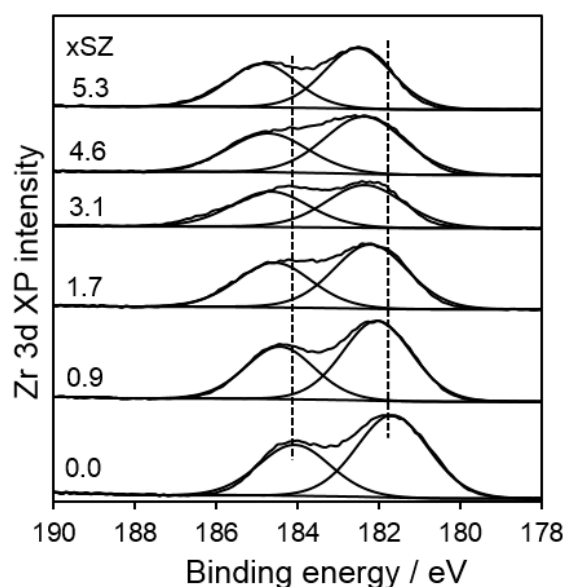
**Figure 3.** Zr 3d XP spectra of parent and sulfated zirconia as a function of bulk S loading.

The SO_4 dispersion was examined from the S 2p:Zr 3d surface ratio (Figure 4) as a function of S loading. This revealed a linear increase for loadings $\leq$1.7 wt %, indicating the growth of a

homogeneous sulfate monolayer. The plateau at interim coverages around 1.7–4.6 wt % suggests that this monolayer is metastable with respect to the formation of SZ multilayers, with additional S incorporated via a change in the nature of the sulfate monolayer (to accommodate a higher SO_4 density). Sulfate multilayer formation is indicated at higher S loadings by a further rise in S:Zr surface ratio. These observations are consistent with the thermal analysis, which indicated a transition in the sulfate adsorption mode around 1.7 wt %. Sulfate monolayer saturation for loadings between 1.7 and 3.1 wt % is in good agreement with that proposed by Osatiashtiani et al. [1], wherein a saturated sulfate monolayer forms around 2.9 wt % following H_2SO_4 impregnation.

Figure 4. S 2p:Zr 3d XP atomic ratio as a function of bulk S loading.

The nature of surface sulfate species was further explored by ex situ FTIR (Figure 5). In accordance with XRD, the parent ZrO_2 shows $\nu_{Zr\text{-}O}$ modes characteristic of m-ZrO_2 at 751 and 413 cm^{-1} [24,25], whose intensity decreases markedly upon sulfation being almost fully attenuated $\geq$1.7 wt %. Modes attributable to t-ZrO_2 at 578 and 502 cm^{-1} [24] were also attenuated following sulfation, but remained clearly visible for all S loadings. Sulfation also caused the δ_{OH} water bending mode (at 1618 cm^{-1}) to sharpen, accompanied by the emergence of strongly overlapping absorptions spanning 1240–960 cm^{-1} arising from $\nu_{S=O}$ and $\nu_{S\text{-}O}$ bond vibrations of surface sulfate. The latter features are most clearly resolved for the 1.7 wt % sample, increasing in intensity but losing resolution at higher S loadings. The consensus is that 1240 and 1142 cm^{-1} bands arise from $\nu_{S=O}$ vibrations in chelating (bridging) bidentate sulfate species coordinated to zirconium cation(s), whereas those at 1076, 1040, and 960 cm^{-1} arise from $\nu_{S\text{-}O}$ vibrations [26,27]. The loss of very weak absorptions at 1458 and 1320 cm^{-1} following sulfation is attributed to displacement of carbonate bound to basic sites on the parent zirconia surface [28,29]. IR frequencies of sulfate species are summarized in Table S1 according to their symmetry. Free sulfate species in dilute solutions assume a T_d structure and hence only exhibit a single $\nu_{S\text{-}O}$ absorption ~1100 cm^{-1}. Complexation of the sulfate ion lowers its symmetry, resulting in IR spectra exhibiting multiple $\nu_{S\text{-}O}$ and $\nu_{S=O}$ absorption bands associated with C_{3v} (species I) and C_{2v} (species II) sulfates in Scheme 1. We propose that the species I and II co-exist for S loadings $\leq$1.7 wt %, characterized by sets of bands at 1142, 1040, and 960 cm^{-1} and 1240 and 1076 cm^{-1} respectively. Pyrosulfate species III and multilayer sulfate species likely dominate at higher S loadings, giving rise to the broad extended absorption over 1000–1300 cm^{-1}. Species II may be only considered as possessing quasi C_{2V} symmetry due to the possible resonance structures shown in Scheme 1.
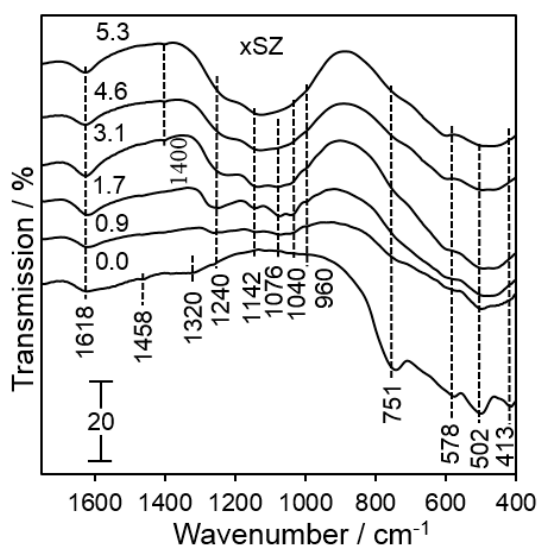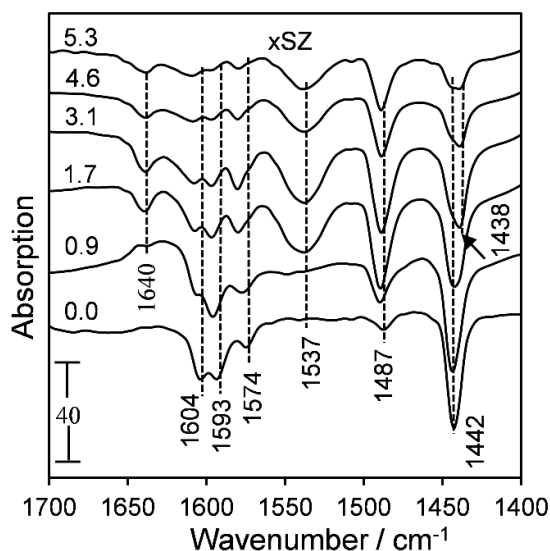
Figure 5. Ex situ FTIR transmission spectra for 550 °C calcined parent and sulfated zirconia as a function of bulk S loading.

2.2. Surface Acidity

Determination of acid-base properties in catalysis should ideally be conducted in operando (or under conditions close to those employed during the catalytic reaction of interest) to permit precise correlation with reactivity. However, identifying appropriate molecular probes and analytical methods amenable to surface acidity/basicity under reaction conditions is extremely challenging, and this typically requires a time-consuming, multi-technique approach combining separation methods with adsorption calorimetry [30]. Here we employed a range of complementary gas phase probes to explore the solid acid/base properties of our materials. While the reaction conditions for such measurements are rather distant from the liquid phase environment present during their application in catalytic esterification, note that all the samples in this work exhibited a degree of surface hydration (evidenced from water desorption by TGA-MS in Table 2 and Figure S1), and hence adsorbed molecular probes encountered a polar surface environment akin to that present during propanoic acid esterification.

In situ FTIR of Py titrated samples was undertaken to probe their acid properties (Figure 6): Py bound to Lewis acid sites (LPy) gives characteristic vibrational bands at 1620–1604, 1580–1570, 1495–1485, and 1445–1440 cm^{-1} [31], whereas Py bound to Brönsted acid sites (BPy) gives characteristic vibrational bands at 1640–1630, 1545–1535, and 1500–1485 cm^{-1} [32]. The 1545–1535 cm^{-1} absorption is considered a fingerprint for BPy, and that at 1445 cm^{-1} a fingerprint for LPy, with their intensities proportional to the acid site density [33]. Physisorbed Py (PPy) and hydrogen-bonded Py (HPy) are often revealed by their desorption in vacuo ≤100 °C [32]. The parent zirconia exhibited LPy, HPy and PPy species, the former a consequence of coordinatively unsaturated Zr^{4+} Lewis acid sites, while surface Zr^{4+}-OH functions may act as hydrogen-bonding sites for HPy species. No Brønsted acid sites were observed for the parent zirconia, in accordance with previous reports [31,34,35]. In contrast, Figure 6 shows that all SZ samples exhibited BPy species (as expected from related literature [6,10]) whose concentration reached a maximum for S loadings between 1.7 and 3.1 wt %. The concentration of LPy species showed a concomitant decrease with S loading, accompanied by a slight blue-shift from 1604 cm^{-1} to 1610 cm^{-1}. Considering the surface structures suggested for surface sulfate (Scheme 1), these observations may be rationalized in terms of Brønsted acid site formation due to monodentate and particularly bridging sulfate (species II). Polymerization of these species at higher sulfate loadings into pyrosulfate (species III) would explain the subsequent loss of Brønsted acidity. High sulfate coverages are expected to site-block Lewis acid (Zr^{4+}) sites to titration by Py molecules, with those remaining accessible displaying enhanced acidity due to the sulfate (electron withdrawing) inductive

effect [10]. The band at 1438 cm^{-1} is attributed to red-shifting of the adsorption band when Py is more weakly coordinated at hindered Lewis acid sites present on the sulfate-rich catalysts (x $\geq$ 1.7 wt %).

Figure 6. In situ FTIR transmission spectra of chemisorbed pyridine on parent and sulfated zirconia as a function of bulk S loading.

IR spectra of room-temperature Py titrated samples subsequently evacuated for 5 min at 100 °C are shown in Figure S3. Both LPy and BPy species were stable to this treatment, with no changes in their respective diagnostic bands at 1488 cm^{-1} and 1539 cm^{-1}. The relative Brönsted:Lewis acid character (I_B/I_L) was determined according to Platon and Thomas [33] from the integrated peak areas of these bands summarized in Table 3 highlights a linear rise in Brönsted character with sulfate loading.

**Table 3.** Surface acidity of parent and sulfated zirconia.

S Loading (wt %)	Brønsted:Lewis Ratio [a]	pH$_{zcp}$	Acid Loading [b] (μmol·g^{-1})	MBOH Conversion [c] (%)
0.0	-	4.68	68	54
0.9	0.05	3.33	282	76
1.7	0.86	2.82	336	90
3.1	1.01	2.90	458	73
4.6	1.13	2.96	362	74
5.3	1.57	2.96	270	59

[a] 1540:1445 cm^{-1} ν_{CCN} bands. [b] Propylamine adsorption and subsequent TGA-MS. [c] IR 3640 cm^{-1} intensity change following 1.3 kPa MBOH exposure at room temperature, heating to 200 °C for 5 min, and cooling to room temperature.

Titration of acid sites via temperature programmed reaction of n-propylamine (n-PA) yielding ammonia and propene gas phase products via Hoffman elimination was also employed to quantify the total surface acidity [36]. Table 3 compares the resulting surface acid loadings with pH$_{zcp}$ values [37]. A suspension of the parent zirconia is moderately acidic (pH = 4.68). Sulfation for loadings 1.7 wt % increased the acidity (pH = 2.82); however, additional surface sulfate did not further increase acidity (pH = 2.96), indicating that the strongest acid sites were associated with surface bisulfate species just prior to saturation of the monolayer [38,39], with pyrosulfate (species III) formed at higher loadings possessing slightly weaker acidity. *N*-propylamine has been described by Gorte and co-workers as a probe for Brønsted acidity [36]; however, n-PA adsorption on Lewis acid sites is also reported [40]. Adsorbed n-PA decomposed to liberate reactively formed propene as shown in Figure S4, and the

corresponding propene desorption temperature and peak intensity are shown in Figure 7, which reveals a maximum in the total surface acid sites for 3.1 wt %. The temperature of n-PA decomposition is characteristic of the acid strength, with lower temperatures indicating the presence of stronger acid sites. Figure 7 shows that the 1.7 wt % exhibited the strongest surface acidity, in excellent agreement with the pH_{zcp} results in Table 3.
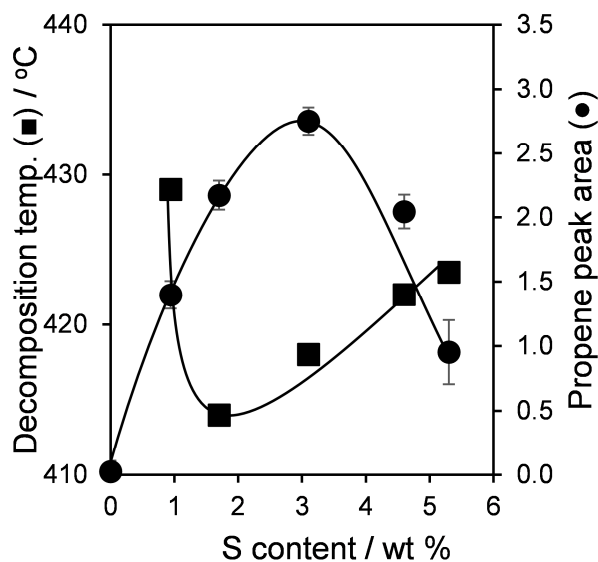

Figure 7. Desorption temperature and peak area for reactively-formed propene from parent and sulfated zirconia as a function of bulk S loading.

Methylbutynol Decomposition

Methylbutynol (MBOH) is an attractive molecule to probe surface acid-base properties of metal oxides [41–43] since the latter strongly influence the product distribution [44]. MBOH decomposition yields acetone and acetylene over basic surfaces, but undergoes dehydration/isomerization over acidic surfaces to 3-methyl-3-buten-1-yne and/or prenal (3-methyl-2-buten-1-ol, $(CH_3)_2C=CH-CHO$); strong Brønsted-Lewis acid pairs are believed necessary to isomerize MBOH to prenal [45]. Amphoteric surfaces decompose MBOH to 3-methyl-3-buten-2-one (MIPK, $CH_3(C=O)-C(CH_3)=CH_2)$) and 3-hydroxy-3-methyl-2-butanone (HMB, $(CH_3)_2C(OH)-(C=O)-CH_3)$) [44]. In this work gas phase in situ IR spectra of the parent zirconia were recorded after exposure to MBOH vapour for 5 min at room temperature (S_{RT}), heating to 200 °C for 5 min, and subsequent cooling to room temperature (S_{200}), as shown in Figure S5. The resulting difference spectrum (S_{200}-S_{RT}) in Figure S5 reveals compositional changes in the gas phase resulting from catalytic reaction of MBOH: negative absorptions are associated with loss of the adsorbed alcohol [44]; positive absorptions arise from reactively-formed products. The S_{RT} of the parent zirconia only exhibited absorptions characteristic of MBOH [44], while the difference spectrum (S_{200}-S_{RT}) showed negative absorptions at 3640, 3330, and 2980 cm^{-1} consistent with loss or conversion of the alcohol, alongside positive absorptions at 3516, 2977, 1728, 1364, and 1183 cm^{-1} indicative of HMB formation [44]. This control experiment confirms the utility of MBOH titration, since it correctly identifies the well-known amphoteric character of pure zirconia. Corresponding difference spectra for SZ samples (Figure 8a) revealed a different set of negative absorptions for all S loadings at 3640, 3330, 2990, 1369, 1324, 1252, 1180, and 1125 cm^{-1} corresponding to loss of MBOH and positive absorptions at 3343, 3325, 3100, 2966, 1810, 1740, 1705, and 1625 cm^{-1}, which we attribute to methylbutyne and prenal formation together with trace acetone [44]. Methylbutyne and acetone were produced for all S loadings, whereas prenal was only observed for S loadings ≥1.7 wt %, suggesting the presence of strong Brønsted-Lewis acid pairs. Acetone formation at low S coverages is consistent

with the presence of basic coordinatively unsaturated O^{2-} species on the predominantly bare zirconia surface in this sub-sulfate monolayer regime.
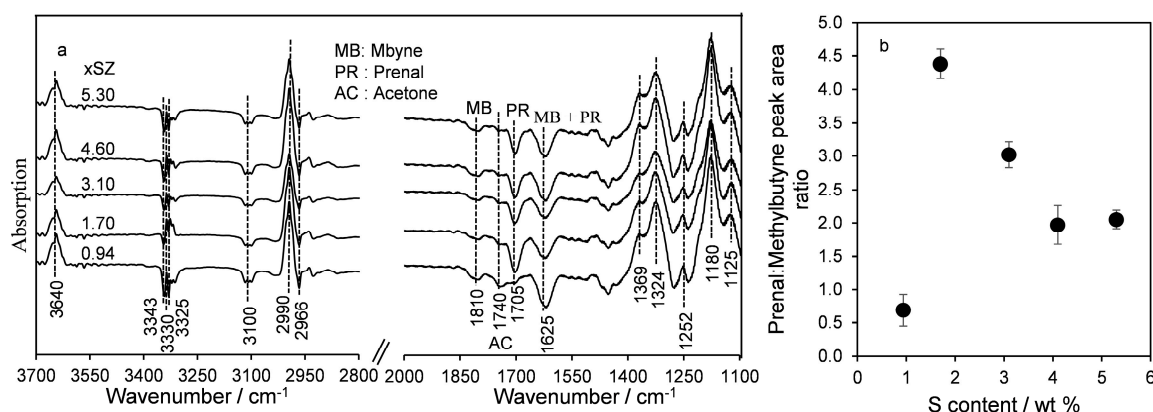
Figure 8. (**a**) IR difference spectra following 1.3 kPa MBOH room temperature MBOH adsorption and subsequent 200 °C heating and cooling, and (**b**) corresponding prenal:methylbutyne peak area as a function of bulk S loading.

Quantitative analysis of the 3640 cm^{-1} band in the IR difference spectra, corrected for appropriate molecular calibrations, gives the MBOH conversion as a function of S loading (Table 3), which increases with sulfation for loadings ≤1.7 wt %, decreasing at higher loadings. The prenal:methylbutyne peak area ratio also exhibits a maximum for 1.7 wt % as shown in Figure 8b, associated with the highest population of strong Brønste-Lewis acid pairs [44]. Table 3 also highlights a strong inverse correlation between MBOH conversion and sample pH, with conversion maximized for the most acidic 1.7 wt % sample (also identified from propylamine decomposition in Figure 7 as the strongest solid acid). Prenal formation, which requires co-existing Lewis and Brønsted acid sites, is favored at intermediate sulfate loadings [44], wherein O^{2-} base sites in the underlying ZrO_2 surface are no longer available, being capped by the sulfate monolayer.
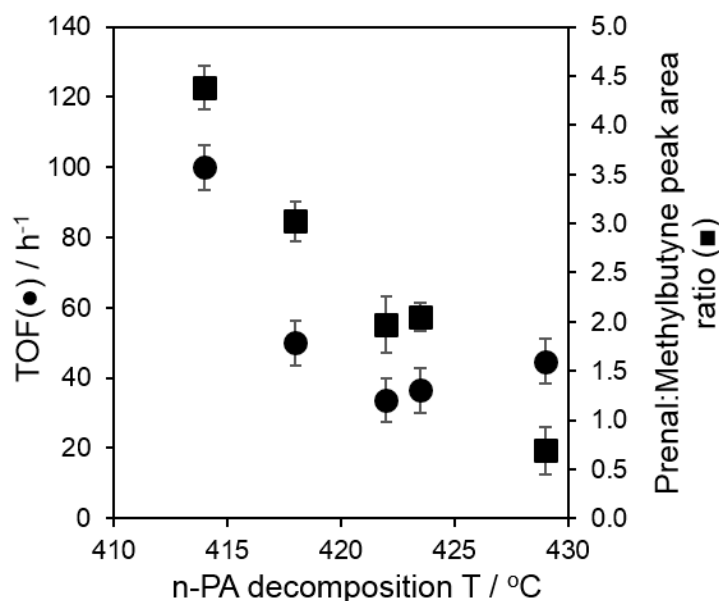
2.3. Catalytic Esterification of Propanoic Acid

The performance of parent and sulfated zirconias was subsequently evaluated for the liquid phase esterification of propanoic acid with methanol. Reaction profiles for propanoic acid conversion are shown in Figure 9a, from which it is obvious that the parent zirconia is essentially inactive. Conversion increased with sulfation for loadings ≤1.7 wt %, falling for higher degrees of sulfation. All catalysts were >98% selective to methyl propanoate. Figure 9b shows the dependence of mass-normalized initial rates of esterification and corresponding turnover frequency (TOF) as a function of S loading, which both exhibit a volcano dependence with maximum for 1.7 wt % corresponding to the maximum concentration of surface bisulfate (species II). A similar TOF value to this maximum was recently reported by Osatiashtiani and co-workers for comparable sulfur content in SZ prepared via H_2SO_4 impregnation [4].

The results display an excellent correlation between the activity for esterification, MBOH conversion, and acid strength (as determined from pH$_{zcp}$ and propylamine decomposition) of our SZ catalysts. Further evidence of the strong correlation between SZ acidity and reactivity is presented in Figure 10, in which esterification activity and prenal formation are both directly proportional to acid strength. Note that increasing the sulfate concentration not only influences surface acidity, but also the degree of surface hydration as determined by TGA-MS (low temperature mass loss and evolved water in Figure 2a, Figure S1 and Table 2). High S loadings therefore enhance the hydrophilicity of our SZ catalysts which is known to suppress fatty acid esterification with methanol due to active site-blocking and/or promotion of the reverse ester hydrolysis reaction [45–47]. Hence the 1.7 wt % catalyst may

deliver maximum esterification performance due to the combination of a high concentration of strong acid sites with significant Brønsted character, and relatively low surface hydrophilicity.
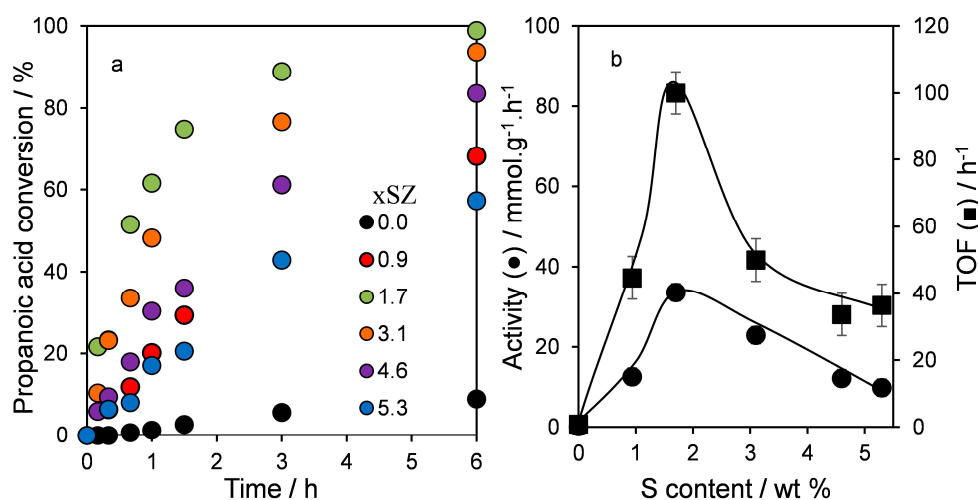

Figure 9. (**a**) Reaction profiles, and (**b**) initial rate and TOF for propanoic acid esterification with methanol over parent and sulfated zirconia catalysts as a function of bulk S loading.

Figure 10. Correlation between TOF for propanoic acid esterification and reactively-formed prenal:methylbutyne ratio over parent and sulfated zirconia as a function of propylamine decomposition temperature.

The stability and recyclability of the most active (1.7 wt %) SZ catalyst for propanoic acid esterification was also assessed. Spent catalyst was recovered by filtration, washing with methanol and drying prior to re-use. Figure S6 shows that this catalyst retained significant activity upon re-use, with conversion only falling to 77% after two recycles, mirroring a similar decrease in initial esterification rate. We attribute this slight loss in esterification performance to partial leaching of sulfate, as evidenced by elemental analysis which revealed the S loading fell to 1.28 wt % after the third reaction, in agreement with previous reports for SZ prepared from H_2SO_4 impregnation [48,49]. Figure 11 also highlights subtle changes in the thermal stability of fresh and spent catalysts, notably

the emergence of a new low temperature SO_2 loss ~630 °C (Figure 11a inset), consistent with the destabilization of sulfate species during esterification, which may promote their leaching.
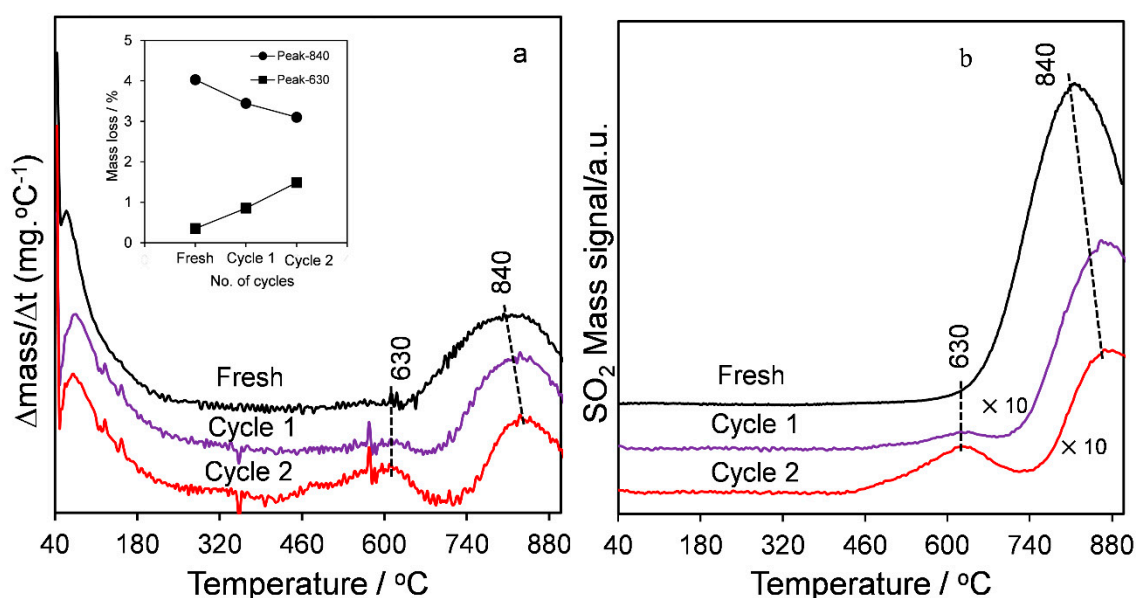
Figure 11. (**a**) DTG profiles, and (**b**) corresponding SO_2 desorption (m/z = 64) for fresh and spent 1.7 wt % SZ.

3. Experimental

3.1. Catalyst Synthesis

A series of sulfated zirconia catalysts (xSZ, where x is the bulk S loading in wt % from CHNS) were prepared by wet impregnation of $Zr(OH)_4$ (XZO 632/3, MEL Chemicals, Manchester, UK) with aqueous solutions of $(NH_4)_2SO_4$ (99.5% purity, Merck, Darmstadt, Germany) of desired molarity, followed by drying and calcination at 550 °C for 3 h. An amount of ammonium sulfate was dissolved in a beaker containing 10 mL deionized water/g-$Zr(OH)_4$ to yield xSZ samples with nominal S loadings spanning 0–7 wt %. The resulting slurry was stirred for 1 h at room temperature overnight, prior to drying at 85 °C for 24 h. Dried materials were subsequently calcined at 550 °C for 3 h in static air and then stored in a desiccator. An unsulfated (parent) zirconia reference was prepared from the hydroxide by an identical calcination treatment.

3.2. Catalyst Characterization

Specific surface areas were determined by N_2 physisorption [50], with samples outgassed at 200 °C for 1 h prior to analysis on a Quantachrome Nova 4200 porosimeter (Quantachrome UK Ltd., Hook, UK). Net surface charge was approximated by determining the zero-charge-point pH value (pH_{zcp}) of solid particles suspended in deionized water (100 mg/20 mL) after 2 h stirring at room temperature using a Jenway 3305 pH meter. Total sulfur content was determined on a Thermos-Scientific Fash 2000 CHNS-O analyser (CE Instruments Ltd., Wigan, UK). Crystalline phase analysis was elucidated by Powder X-ray diffraction (XRD) using a Bruker D8 Advance Diffractometer with a LynxEye high-speed strip detector and Cu Kα (1.54 Å) radiation fitted with a Ni filter and calibrated against a quartz reference (Bruker Ltd., Coventry, UK). The crystalline phases were identified in comparison with relevant literature [1,7]

Surface compositions was determined via XPS using a Kratos Axis HSi spectrometer equipped with a charge neutralizer, a monochromated Al Kα source (1486.7 eV) and magnetic focusing lens (Kratos Analytical Ltd., Manchester, UK). Spectra were recorded at normal emission with a pass

energy of 40 eV under a vacuum of 1.3×10^{-11} kPa, with binding energies referenced to adventitious carbon C1s at 284.6 eV. Curve fitting of XPS spectra was carried out using CasaXPS version 2.3.15. The nature, amount and thermal stability of sulfoxy species was also probed by coupled thermogravimetric analysis-mass spectrometry (TGA-MS) measurements (Pfeiffer Vacuum GmbH, Asslar, Germany and Mettler-Toledo Ltd., Leicester, UK), and ex/in situ Fourier-transform infrared spectroscopy (FTIR, Mattson Thermal Products GmbH, Daimlerstraße, Germany). TGA-MS were performed on a Mettler Toledo STAR^e TGA-MS analyzer linked to a Pfeiffer Vacuum ThermoStar^{TM} GSD 301 T3 mass spectrometer. Ex/in situ FTIR spectra were measured on a Thermo Mattson Genesis II FT-IR spectrometer; spectra were recorded at 4000–400 cm^{-1} at 4 cm^{-1} resolution. Ex situ spectra were recorded in transmission on ~1 wt % samples as supported KBr discs. In situ spectra were recorded in a bespoke Pyrex IR cell (with CaF$_2$ windows), similar to that described by Peri and Hannan [51]. Pyridine (Py) adsorption/desorption experiments were performed on self-supporting thin wafers of sample (~25 mg·cm^{-2}) mounted inside the cell and pretreated via: (i) heated under 50 cm^3·min^{-1} O$_2$ at 400 °C for 30 min; (ii) degassing at 400 °C in vacuo for 30 min; and (iii) cooling to room temperature in vacuo. Spectra were recorded before and after 5-min exposure to 1.3 kPa of Py vapor (followed by degassing at RT and 100 °C). Difference spectra of adsorbed Py species were obtained by subtraction of the background spectrum. Py vapor (Specpure BDH) was dosed into the cell via expansion of the liquid previously purified via in-line freeze-pump-thaw cycles. Temperature-programmed decomposition of propylamine decomposition to propene and NH$_3$ via the Hoffman elimination reaction was employed to quantify acid loading and strength. n-Propylamine (≥99%, Sigma Aldrich, Irvine, UK) was added by pipette to samples which were then dried for 2 h, and physisorbed propylamine removed by degassing at 30 °C overnight in vacuo. Samples were then heated in the TGA furnace under flowing N$_2$ (30 cm^3·min^{-1}) from 40–1000 °C at a ramp rate of 10 °C·min^{-1}. MS signals at 18, 64 and 80 amu were followed to quantify evolved H$_2$O, SO$_2$, and SO$_3$, respectively.

Methylbutynol (MBOH) conversion was studied in a bespoke IR reaction cell in which ~100 mg of sampled was placed. IR spectra were recorded during exposure of the sample to 1.3 kPa of alcohol vapour before and after heating at 200 °C for 5 min. Difference spectra were obtained by subtraction of the alcohol background spectra. Prior to analysis, samples were pretreated as described for the Py experiments above, employing vapor from MBOH liquid (Merck) purified by freeze-pump-thaw cycles. In situ IR spectra were recorded at room temperature under identical optical conditions.

3.3. Catalytic Esterification

Propanoic acid esterification with methanol was performed under stirred batch conditions at atmospheric pressure in a Radleys Carousel reaction station in 25-mL glass boiling tubes. Reactions were conducted with 5 mmol propanoic acid in 6.07 mL of methanol (MeOH:acid = 30:1 molar ratio) at 60 °C with 100 mg catalyst and 0.5 mmol of dihexyl ether as an internal standard. Reaction profiles were obtained via periodic sampling and analysis on a Shimadzu GC-2010 (Shimadzu UK Ltd., Wolverton, UK) equipped with a ZB-50 capillary column (30 m × 0.32 mm × 0.25 μm). Analyses were performed in triplicate. Turnover frequencies (TOFs) were determined from the linear portion of the initial reaction profile (<25% acid conversion), with rates normalized to the total acid site density determined from propylamine decomposition. Catalyst recyclability was assessed for two consecutive reactions: after 6 h reaction, the catalyst was recovered by filtration, washed with methanol, and then re-used under identical conditions. Errors in GC conversion and product yield are quoted ±2%.

4. Conclusions

A family of SZ catalysts with systematically increasing SO$_4$ content were successfully prepared by wet impregnation with an (NH$_4$)SO$_4$ precursor. Isolated, tridentate sulfate ((ZrO)$_3$-S=O) species dominate for low S loadings <1.7 wt %, with induced Brønsted acidity arising from adjacent Zr^{4+}–OH groups. At intermediate sulfur loadings (1.7–3.1 wt %), bisulfate-like ((ZrO)$_2$(OH)(S=O)) species predominate, which exhibit superacidity arising from delocalized protons in S-OH moieties. At higher

S content, Brønsted acidity decreases due to pyrosulfate/multilayer formation. Methylbutynol (MBOH) was successfully demonstrated as a reactive probe molecule to follow the evolution of SZ acid properties as a function of sulfate coverage. Bifunctional catalysts are generated at low S content, exhibiting amphoteric character arising from Lewis base and Brønsted acid sites likely associated with coordinatively unsaturated O^{2-} and Zr^{4+}-OH species, respectively, whereas strong Brønsted-Lewis acid pairs form at intermediate S loadings. The relative Brønsted:Lewis acid character is directly proportional to the degree of surface sulfation.

Catalytic activity of SZ for propionic acid esterification with methanol is a strong function of solid acid strength, with optimum activity associated with the formation of a saturated sulfate monolayer comprising monomeric, chelating/bridging bisulfate species (which exhibit both strong Brønsted acidity and co-operative Brønsted-Lewis acidity from MBOH reactive titration). The optimum 1.7 wt % SZ catalyst retains good activity (~77% conversion in 6 h) after two recycles, with a small degree of S leaching attributable to the destabilization of surface sulfate during reaction.

Conflicts of Interest: the authors declare no conflict of interest.

References

1. Osatiashtiani, A.; Lee, A.F.; Brown, D.R.; Melero, J.A.; Morales, G.; Wilson, K. Bifunctional SO_4/ZrO_2 catalysts for 5-hydroxymethylfufural (5-HMF) production from glucose. *Catal. Sci. Technol.* **2014**, *4*, 333–342. [CrossRef]

2. Jung, K.T.; Bell, A.T. Effects of catalyst phase structure on the elementary processes involved in the synthesis of dimethyl carbonate from methanol and carbon dioxide over zirconia. *Top. Catal.* **2002**, *20*, 97–105. [CrossRef]

3. Suwannakarn, K.; Lotero, E.; Goodwin, J.G.; Lu, C. Stability of sulfated zirconia and the nature of the catalytically active species in the transesterification of triglycerides. *J. Catal.* **2008**, *255*, 279–286. [CrossRef]

4. Osatiashtiani, A.; Durndell, L.J.; Manayil, J.C.; Lee, A.F.; Wilson, K. Influence of alkyl chain length on sulfated zirconia catalysed batch and continuous esterification of carboxylic acids by light alcohols. *Green Chem.* **2016**, *18*, 5529–5535. [CrossRef]

5. Yadav, G.; Sengupta, S. Friedel-crafts alkylation of diphenyl oxide with benzyl chloride over sulphated zirconia. *Org. Proc. Res. Dev.* **2002**, *6*, 256–262. [CrossRef]

6. Tabora, J.E.; Davis, R.J. On the superacidity of sulfated zirconia catalysts for low-temperature isomerization of butane. *J. Am. Chem. Soc.* **1996**, *118*, 12240–12241. [CrossRef]

7. Ecormier, M.A.; Wilson, K.; Lee, A.F. Structure-reactivity correlations in sulphated-zirconia catalysts for the isomerisation of α-pinene. *J. Catal.* **2003**, *215*, 57–65. [CrossRef]

8. Ahmed, I.; Khan, N.A.; Mishra, D.K.; Lee, J.S.; Hwang, J.-S.; Jhung, S.H. Liquid-phase dehydration of sorbitol to isosorbide using sulfated titania as a solid acid catalyst. *Chem. Eng. Sci.* **2013**, *93*, 91–95. [CrossRef]

9. Yadav, G.D.; Nair, J.J. Sulfated zirconia and its modified versions as promising catalysts for industrial processes. *Microporous Mesoporous Mater.* **1999**, *33*, 1–48. [CrossRef]

10. Jin, T.; Yamaguchi, T.; Tanabe, K. Mechanism of acidity generation on sulfur-promoted metal oxides. *J. Phys. Chem.* **1986**, *90*, 4794–4796. [CrossRef]

11. Babou, F.; Coudurier, G.; Vedrine, J.C. Acidic properties of sulfated zirconia: An infrared spectroscopic study. *J. Catal.* **1995**, *152*, 341–349. [CrossRef]

12. Chen, F.; Coudurier, G.; Joly, J.-F.; Vedrine, J. Superacid and catalytic properties of sulfated zirconia. *J. Catal.* **1993**, *143*, 616–626. [CrossRef]

13. Arata, K.; Hino, M. Preparation of superacids by metal oxides and their catalytic action. *Mater. Chem. Phys.* **1990**, *26*, 213–237. [CrossRef]

14. Clearfield, A.; Serrette, G.; Khazi-Syed, A. Nature of hydrous zirconia and sulfated hydrous zirconia. *Catal. Today* **1994**, *20*, 295–312. [CrossRef]

15. Venkatesh, K.R.; Hu, J.; Dogan, C.; Tierney, J.W.; Wender, I. Sulfated metal oxides and related solid acids: Comparison of protonic acid strengths. *Energy Fuels* **1995**, *9*, 888–893. [CrossRef]

16. Bensitel, M.; Saur, O.; Lavalley, J.-C.; Morrow, B. An infrared study of sulfated zirconia. *Mater. Chem. Phys.* **1988**, *19*, 147–156. [CrossRef]

17. Morterra, C.; Cerrato, G.; Bolis, V. Lewis and brønsted acidity at the surface of sulfate-doped ZrO_2 catalysts. *Catal. Today* **1993**, *17*, 505–515. [CrossRef]

18. Stichert, W.; Schüth, F. Synthesis of catalytically active high surface area monoclinic sulfated zirconia. *J. Catal.* **1998**, *174*, 242–245. [CrossRef]

19. Stichert, W.; Schüth, F.; Kuba, S.; Knözinger, H. Monoclinic and tetragonal high surface area sulfated zirconias in butane isomerization: Co adsorption and catalytic results. *J. Catal.* **2001**, *198*, 277–285. [CrossRef]

20. Son, J.R.; Gwon, T.D.; Kim, S.B. Characterization of zirconium sulfate supported on zirconia and activity for acid catalysis. *Bull. Korean Chem. Soc.* **2001**, *22*, 1309–1315.

21. Reddy, B.M.; Patil, M.K. Organic syntheses and transformations catalyzed by sulfated zirconia. *Chem. Rev.* **2009**, *109*, 2185–2208. [CrossRef] [PubMed]

22. Walrafen, G.; Irish, D.; Young, T. Raman spectral studies of molten potassium bisulfate and vibrational frequencies of S_2O_7 groups. *J. Chem. Phys.* **1962**, *37*, 662–670. [CrossRef]

23. Moulder, J.F.; Stickle, W.F.; Sobol, P.E.; Bomben, K.D. *Handbook of X-ray Photoelectron Spectroscopy: A Reference Book of Standard Spectra for Identification and Interpretation of Xps Data*, 3rd ed.; Physical Electronics Eden Prairie: Chanhassen, MN, USA, 1992; p. 109.

24. Chen, S.; Yin, Y.; Wang, D.; Liu, Y.; Wang, X. Structures, growth modes and spectroscopic properties of small zirconia clusters. *J. Cryst. Growth* **2005**, *282*, 498–505. [CrossRef]

25. Qian, Z.; Shi, J. Characterization of pure and doped zirconia nanoparticles with infrared transmission spectroscopy. *Nanostruct. Mater.* **1998**, *10*, 235–244. [CrossRef]

26. Mishra, M.K.; Tyagi, B.; Jasra, R.V. Synthesis and characterization of nano-crystalline sulfated zirconia by sol-gel method. *J. Mol. Catal. A-Chem.* **2004**, *223*, 61–65. [CrossRef]

27. Deshmane, V.G.; Adewuyi, Y.G. Mesoporous nanocrystalline sulfated zirconia synthesis and its application for ffa esterification in oils. *Appl. Catal. A-Gen.* **2013**, *462*, 196–206. [CrossRef]

28. Köck, E.-M.; Kogler, M.; Bielz, T.; Klötzer, B.; Penner, S. In situ FT-IR spectroscopic study of CO_2 and CO adsorption on Y_2O_3, ZrO_2, and yttria-stabilized ZrO_2. *J. Phys. Chem. C* **2013**, *117*, 17666–17673. [CrossRef] [PubMed]

29. Dobson, K.D.; McQuillan, A.J. An infrared spectroscopic study of carbonate adsorption to zirconium dioxide sol-gel films from aqueous solutions. *Langmuir* **1997**, *13*, 3392–3396. [CrossRef]

30. Carniti, P.; Gervasini, A.; Biella, S.; Auroux, A. Intrinsic and effective acidity study of niobic acid and niobium phosphate by a multitechnique approach. *Chem. Mater.* **2005**, *17*, 6128–6136. [CrossRef]

31. Hess, A.; Kemnitz, E. Surface acidity and catalytic behavior of modified zirconium and titanium dioxides. *Appl. Catal. A-Gen.* **1997**, *149*, 373–389. [CrossRef]

32. Zaki, M.I.; Hasan, M.A.; Al-Sagheer, F.A.; Pasupulety, L. In situ ftir spectra of pyridine adsorbed on SiO_2-Al_2O_3, TiO_2, ZrO_2 and CeO_2: General considerations for the identification of acid sites on surfaces of finely divided metal oxides. *Colloids Surf. A Physicochem. Eng. Asp.* **2001**, *190*, 261–274. [CrossRef]

33. Platon, A.; Thomson, W.J. Quantitative lewis/brönsted ratios using drifts. *Ind. Eng. Chem. Res.* **2003**, *42*, 5988–5992. [CrossRef]

34. Waqif, M.; Bachelier, J.; Saur, O.; Lavalley, J.-C. Acidic properties and stability of sulfate-promoted metal oxides. *J. Mol. Catat.* **1992**, *72*, 127–138. [CrossRef]

35. Matsuhashi, H.; Motoi, H.; Arata, K. Determination of acid strength of solid superacids by temperature programmed desorption using pyridine. *Catal. Lett.* **1994**, *26*, 325–328. [CrossRef]

36. Farneth, W.; Gorte, R. Methods for characterizing zeolite acidity. *Chem. Rev.* **1995**, *95*, 615–635. [CrossRef]

37. Bourikas, K.; Vakros, J.; Kordulis, C.; Lycourghiotis, A. Potentiometric mass titrations: Experimental and theoretical establishment of a new technique for determining the point of zero charge (PZC) of metal (HYDR) oxides. *J. Phys. Chem. B* **2003**, *107*, 9441–9451. [CrossRef]

38. Kustov, L.; Kazansky, V.; Figueras, F.; Tichit, D. Investigation of the acidic properties of ZrO_2 modified by SO_4^{2-} anions. *J. Catal.* **1994**, *150*, 143–149. [CrossRef]

39. Adeeva, V.; Dehaan, J.; Janchen, J.; Lei, G.; Schunemann, V.; Vandeven, L.; Sachtler, W.; Vansanten, R. Acid sites in sulfated and metal-promoted zirconium dioxide catalysts. *J. Catal.* **1995**, *151*, 364–372. [CrossRef]

40. Penzien, J.; Abraham, A.; van Bokhoven, J.A.; Jentys, A.; Müller, T.E.; Sievers, C.; Lercher, J.A. Generation and characterization of well-defined Zn^{2+} lewis acid sites in ion exchanged zeolite bea. *J. Phys. Chem. B* **2004**, *108*, 4116–4126. [CrossRef]

41. Audry, F.; Hoggan, P.; Saussey, J.; Lavalley, J.; Lauron-Pernot, H.; Le Govic, A. Infrared study and quantum calculations of the conversion of methylbutynol into hydroxymethylbutanone on zirconia. *J. Catal.* **1997**, *168*, 471–481. [CrossRef]

42. Lauron-Pernot, H.; Luck, F.; Popa, J. Methylbutynol: A new and simple diagnostic tool for acidic and basic sites of solids. *Appl. Catal.* **1991**, *78*, 213–225. [CrossRef]

43. Lauron-Pernot, H. Evaluation of surface acido-basic properties of inorganic-based solids by model catalytic alcohol reaction networks. *Catal. Rev.* **2006**, *48*, 315–361. [CrossRef]

44. Mekhemer, G.A.; Zaki, M.I. In situ ftir spectroscopic assessment of methylbutynol catalytic conversion products in relation to the surface acid-base properties of systematically modified aluminas. *Surf. Sci.* **2016**, *652*, 269–277. [CrossRef]

45. Dacquin, J.-P.; Cross, H.E.; Brown, D.R.; Duren, T.; Williams, J.J.; Lee, A.F.; Wilson, K. Interdependent lateral interactions, hydrophobicity and acid strength and their influence on the catalytic activity of nanoporous sulfonic acid silicas. *Green Chem.* **2010**, *12*, 1383–1391. [CrossRef]

46. Satyarthi, J.K.; Srinivas, D.; Ratnasamy, P. Influence of surface hydrophobicity on the esterification of fatty acids over solid catalysts. *Energy Fuels* **2010**, *24*, 2154–2161. [CrossRef]

47. Lee, A.F.; Bennett, J.A.; Manayil, J.C.; Wilson, K. Heterogeneous catalysis for sustainable biodiesel production via esterification and transesterification. *Chem. Soc. Rev.* **2014**, *43*, 7887–7916. [CrossRef] [PubMed]

48. Corma, A. Solid acid catalysts. *Curr. Opin. Solid St. Mater. Sci.* **1997**, *2*, 63–75. [CrossRef]

49. Kiss, A.A.; Dimian, A.C.; Rothenberg, G. Solid acid catalysts for biodiesel production-towards sustainable energy. *Adv. Synth. Catal.* **2006**, *348*, 75–81. [CrossRef]

50. Brunauer, S.; Emmett, P.H.; Teller, E. Adsorption of gases in multimolecular layers. *J. Am. Chem. Soc.* **1938**, *60*, 309–319. [CrossRef]

51. Peri, J.B.; Hannan, R.B. Surface hydroxyl groups on γ-alumina1. *J. Phys. Chem.* **1960**, *64*, 1526–1530. [CrossRef]